Pharmaceutical Sciences and Drug Design
ISSN: 3062-4428
2026, Volume 6, Issue 1, Page No: 152-168

Available online at: www.galaxypub.co/page/journals

Galaxy Publication

Molecular Docking and Binding Mechanism Analysis of Levofloxacin Structural Derivatives with DNA Gyrase and Topoisomerase IV

Nguyen Thanh Huy[1]*, Pham Quang Minh[1], Le Thi Bich[2]

[1]Department of Pharmaceutical Sciences and Drug Discovery, Faculty of Pharmacy, Vietnam National University, Hanoi, Vietnam.
[2]Department of Drug Engineering and Therapeutics, Faculty of Medicine, Can Tho University, Can Tho, Vietnam.

***E-mail** ✉ huy.nguyen@gmail.com

Received: 16 December 2025; **Revised:** 17 March 2026; **Accepted:** 26 March 2026

ABSTRACT

Persistent microbial antibiotic resistance, together with the growing frequency of pandemics, fuels the demand for new antimicrobial agents (AntAg). Given the AntAg shortfall, studies aimed at developing rapid strategies for identifying novel drug candidates are highly relevant. The present investigation is designed to carry out an in silico examination of the biological activity spectrum along with the molecular binding interactions of four structurally distinct levofloxacin (Lvf) variants engaging bacterial type IIA topoisomerase targets (DNA gyrase and topoisomerase IV), with the broader aim of aiding the creation of pharmaceuticals possessing an improved safety profile characterization. A suite of computational tools was harnessed for this purpose, notably ChemicPen v. 2.6, PyMol 2.5, Avogadro 1.2.0, PASS, and AutoDockTools 1.5.7 paired with the next-generation engine Autodock Vina. Collectively, these applications represent a pioneering set, made accessible for cluster visualization, featuring ligand-receptor binding affinity quantification, clustering coordinates, and hypothesized mechanisms of action. One authentic Lvf structure, specifically a decarboxylated derivative, was generated through tribochemical (TrbCh) treatment. The range of molecular ligand activity is depicted using a Bayesian probability-based activity estimation model (PASS software, Version 2.0). Both predicted and real (PMS and RMS) molecular configurations of Lvf, arranged in descending order of structural complexity, were encoded using Wiener (W), Balaban (Vs), Detour (Ip), and Electropy indices. Two-dimensional «structure-activity» plots served to discriminate among closely analogous levofloxacin forms. PMS and RMS were rendered as three-dimensional models of the respective ligand-receptor assemblies. The interfacial zones where RMS and PMS engage crucial amino acid residues—namely SER-79, DT-15, DG-1, DA-1—were illustrated. Details on intra- and intermolecular contact regions, free energy values (affinity, expressed in kcal/mol), the binding constant Kb (M−1), and the total cluster count are provided. The findings yielded by this in silico methodology for exploring the spectrum of action, establishing quantitative “structure-activity” relationships, and forecasting molecular mechanisms may prove to be of applied value for targeted drug development.

Keywords: In silico methods, Topological indices, Pa/Pi ratios, Molecular docking, Free energy of binding, Type IIA topoisomerases targets

How to Cite This Article: Huy NT, Minh PQ, Bich LT. Molecular Docking and Binding Mechanism Analysis of Levofloxacin Structural Derivatives with DNA Gyrase and Topoisomerase IV. Pharm Sci Drug Des. 2026;6(1):152-68. https://doi.org/10.51847/dHWrNIIUvt

Introduction

Fluoroquinolones (FlrQs) constitute a class of broad-spectrum chemotherapeutic substances active against Gram-positive and Gram-negative aerobic bacteria, chlamydia, and mycoplasmas. Their debut in clinical settings dates to the 1980s [1]. Even though FlrQs are considered essential reserve medications, their therapeutic status remains a subject of debate. Instrumental in this discourse were the 2018 safety communications disseminated by the Food and Drug Administration (FDA) and the European Medicines Agency (EMA), which highlighted disabling adverse drug reactions (ADRs) linked to FlrQs involving the aorta, peripheral vasculature, articular structures,

and the central nervous system [2]. Despite these concerns, the COVID-19 pandemic triggered a pronounced revival of interest in FlrQs, driven by an antimicrobial drug deficit (roughly 63%) needed to avert post-viral disease complications [3].

Fluoroquinolones are stratified into generations (1G–5G) according to their biological activity breadth, which is a function of structural differentiation (QSAR effect). The attachment of a fluorine atom at position C6 onto the 1G fluoroquinolone framework—exemplified by nalidixic, oxolinic, and pipemidic acids, all derived from the antimalarial chloroquine—gave rise to 2G agents exhibiting an extended antibacterial spectrum (ciprofloxacin, norfloxacin, ofloxacin, pefloxacin, lomefloxacin) **(Figure 1)** [4, 5].

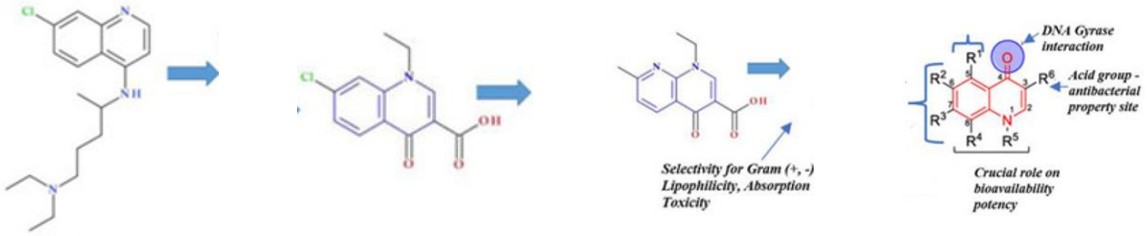

a) b) c) d)

Figure 1. Evolution of the core structures of quinolone class drugs. (a) chloroquine; (b) chloro−l−ethyl−l,4−dihydro−4−oxoquinoline−3-carboxylic acid; (c) nalidixic acid; (d) FlrQs general structure. R1 = H, OH, CH3 or −NH2; R3 = piperazine, piperidin, pyrrolidine or azepin; R4 = CCl, CF, COMe, CHn, R5 = Alk or homocycle; R6 = COOH; R2 = Hal, CN, Alk; R4 = CCl, CF, COMe, CHn.

It is presently recognized that the chief pharmacophoric element within FlrQs is a central bicyclic nucleus bearing a hydrogen at C2, a carboxyl moiety at C3, and a ketone functionality at C4. Substituents decorating positions C7 and C8 profoundly modulate the potency, therapeutic coverage, and safety attributes of FlrQs **(Figure 1d).** The prevailing view [6] holds that the coupling of R7 and R8 to subunit "A" of the DNA-enzyme complex steers the biological effect orientation of this pharmaceutical category.

QSAR methodologies form the cornerstone of FlrQ's structural refinement. Appending a second fluorine atom at C8 while expanding the count of homo- and heterocyclic rings culminated in 3G derivatives (sparfloxacin, levofloxacin). Further structural elaboration via replacement of the piperazine ring with a pyrrolidine ring and the addition of an ester moiety spawned 4G derivatives (moxifloxacin, gemifloxacin). This generation features a protracted, dose-contingent pathway to microbial resistance development, minimal inhibitory concentration values (MIC-90 ≤ 0.25 mg·L−1), and utility in managing nosocomial infections [7-9]. Nonetheless, the escalating complexity of drug molecular architectures sits at odds with the "ideal drug" paradigm, thereby eroding the interplay among efficacy, safety, selectivity, side-effect mitigation, and therapeutic index expansion.

Earlier computational modeling efforts have revealed that the C-3/C-4 zone of quinolone keto acids undergoes chelation by a non-catalytic magnesium ion, which in turn is held in place by four surrounding water molecules. Resistance-associated mutations in DNA gyrase, frequently identified in drug-resistant bacterial strains, are presumed to arise within amino acid residues that form components of the water–metal ion bridging network connecting the enzyme to the pharmaceutical agent [10].

Beyond this, the rise of quinolone resistance across multiple bacterial pathogens has become clinically significant: resistant phenotypes have now been confirmed in Streptococcus pneumoniae and methicillin-resistant Staphylococcus aureus (MRSA) isolates [11].

A compilation of both measured and computationally estimated data describing FlrQ characteristics across the 1G through 5G generations is provided in **Table 1**, offering a means to follow how properties shift in a structure-dependent fashion.

Table 1. Chemical, physical, and biological quinolone properties values.

Molecular Weight, g·mol^{-1}	Log P_o/w	pKa (Strongest Acidic)	Water Solubility, mg·mL^{-1}	Toxicity in mice LD50, mg·kg^{-1}	Microbiological activity/Indications
Nalidixic acid (FlrQ-1G)					

232.2	1.6	8.60	0.1	4000	Enterobacteriaceae/ Uncomplicated urinary tract infections, unsuitable for systemic infections *
Ciprofloxacin (FlrQ-2G)					
331.3	0.3	6.10	<1.00	2000	Enterobacteriaceae, atypical pathogens; *Pseudomonas aeruginosa*, Pneumococci/ *, as well as complicated urinary tract and catheter-linked infections, gastroenteritis
Levofloxacin (FlrQ-3G)					
361.4	0.7	5.50	1.44	1800	Enterobacteriaceae, atypical pathogens, and streptococci. Pneumococci MIC90: 0.25–0.5 mg·L^{-1}/ * also community-acquired pneumonia among hospitalized patients or when atypical pathogens are strongly suspected
Moxifloxacin (FlrQ-4G)					
401.4	2.9	5.49	1.15	100	Enterobacteriaceae, *P. aeruginosa*, atypical pathogens, MSSA, streptococci, anaerobes, Pneumococci. May be considered for managing intra-abdominal infections
Levonadifloxacin (FlrQ-5G)					
360.4	0.87 **	5.94 **	0.63 **	535 **	Active against MDR, MRSA, MDR *S. pneumoniae*, ESKAPE pathogens, *P. aeruginosa*, and *S. aureus* strains/ hospital-acquired and nosocomial pneumonia, diabetic foot ulcer infections, and skin and soft tissue infections, acute otitis externa (swimmer's ear)

—uncomplicated urinary tract infections, not for use in systemic infections, —predicted.

Continuing progress in the field of combinatorial chemistry has paved the way for a fresh set of FlrQs (5G) that received regulatory clearance from both the FDA and EMA within the last ten years—these include nemonoxacin, finafloxacin, zabofloxacin, levonadifloxacin, lascufloxacin, and delafloxacin. Members of this fluoroquinolone cohort have shown strong efficacy against penicillin-resistant and multidrug-resistant (MDR) pneumococcal strains, as well as anaerobic microbes, while preserving potency against aerobic organisms [12]. What sets the FlrQs and quinolones QNs (5G) apart structurally from earlier generations is the presence of anywhere from a single fluorine up to three fluorine substituents (as in lascufloxacin), mixed halogenation with both fluorine and chlorine atoms (exemplified by delafloxacin), or the total elimination of halogen substituents, a feature observed in nemonoxacin, along with several stereogenic centers that dictate the optical behavior and pharmacological profiles of individual isomers **(Figure 2)** [13].

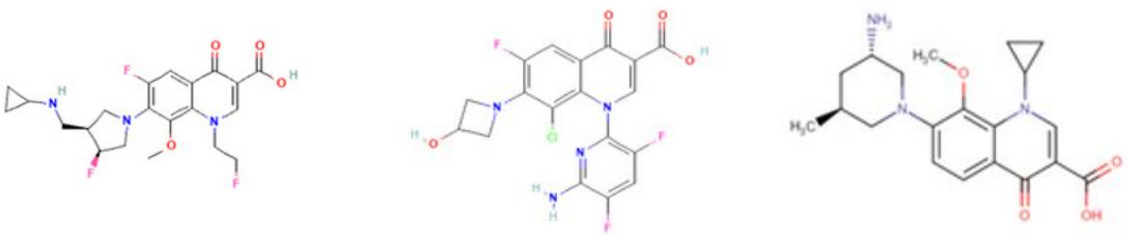

a) b) c)

Figure 2. Chemical structure of newer approved antibacterial QN (5G): (a) lascufloxacin, (b) delafloxacin, and (c) nemonoxacin.

With the emergence of novel FlrQs, documented instances wherein this category of compounds manifests "non-classical" biological functions—spanning anti-HIV-1 integrase effects [14], cannabinoid receptor-2 agonist/antagonist behavior [15], anxiolytic properties, antiischemic actions, and antiviral capabilities, among others—are consistently reigniting scientific enthusiasm for this chemical scaffold [16]. Such findings highlight the need to probe the inherent correlation in the "structure-activity" relationship. This interplay is underpinned by diverse mechanisms governing the low-molecular-weight biological actions of quinolone family xenobiotics. Ultimately, the observed activity is dictated by the chemical nature and three-dimensional positioning of functional substituents.

A well-established strategy for devising new therapeutic agents with improved pharmacokinetic and pharmacodynamic properties entails isolating and characterizing metabolites generated by the biotransformation pathways of an existing drug. Under this paradigm, the parent compound fulfills the role of a prodrug. Fluoroquinolones are subject to biochemical alteration only to a relatively modest degree. Their chief metabolic products include demethylated variants, N-oxide forms, and formyl conjugates, none of which display meaningful pharmacological action. Levofloxacin is primarily eliminated renally in its original, unmodified state [17].

Against this backdrop, the value of innovative approaches for simulating the biological behavior of chemical substances continues to grow. Such approaches involve direct modeling techniques to reconstruct the three-dimensional architecture of ligand-receptor assemblies, coupled with assessments of conformation and reciprocal affinity using in silico QSAR and molecular docking methodologies. De novo design, which strives to piece together a hypothetical blueprint of target molecular structures, makes it feasible to configure low-molecular-weight ligand orientations within the receptor's active binding cleft. This outcome is achieved through the simultaneous reduction of inter-group repulsive forces (steric considerations) and the enhancement of overall binding energetics [18].

The central purpose of the present investigation is to harness in silico tools to examine biological activity and the trends governing alterations in properties across different molecular graphs, while also predicting molecular-level binding interactions of levofloxacin structural variants with bacterial type IIA topoisomerase.

Materials and Methods

Fluoroquinolone samples

Featured in this study is a pharmaceutical-grade levofloxacin hemihydrate (Lvf·1/2 H_2O) substance of high purity (≥99.9%), sourced from Jiangsu Aimi Tech Co., Ltd. (Jiangsu, China) **(Figure 3).**

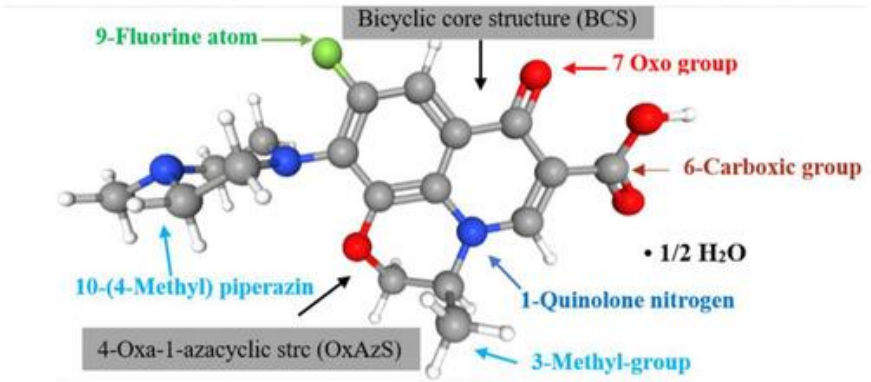

(3*S*)-9-Fluoro-3-methyl-10-(4-methylpiperazin-1-yl)-7-oxo-2,3-dihydro-7*H*-pyrido[1,2,3-*de*][1,4]benzoxazine-6-carboxylic acid hemihydrate

Figure 3. 3D chemical structure depiction of levofloxacin hemihydrate [19].

QSAR

Estimation of biological activity was carried out through Quantitative Structure-Activity Relationships (QSAR) evaluation of PMS and RMS configurations within the CHP and MOL, ChemDesk environments, making use of the ChemicPen v. 2.6 software package (https://cetramax-chemicpen.software.informer.com, accessed on 21 October 2022) [20]. Both real and predicted molecular arrangements (RMS and PMS) were transformed into a unified set of characteristic structural descriptors employing numerical (topological) indices (TI): Wiener (W),

Balaban (Bc), Detour (Ip), and Electropy (E). These indices collectively capture a range of physicochemical and biological features inherent to molecular graphs **(Table 2)** [21].

Table 2. Topological indices.

Topological index	Description	Formula
Wiener (W)	The total sum of shortest path distances taken across every pair of vertices within the graph G	W=0.5$\sum_{i=1}^{n}\sum_{j=1}^{n}$(d)ij where *dij* stands for the shortest distance separating vertex i from vertex j
Balaban (J)	The mean distance-sum connectivity descriptor	$J=\frac{m}{m-n+2}\sum_{uv\epsilon E(G)}\frac{1}{\sqrt{w(u)\cdot w(v)}}$ where n and m correspond to the number of vertices and the number of edges of G, respectively, and w(u) (resp. w(v))represents the cumulative sum of distances from vertex u (resp. v) to every remaining vertex within G
Detour (Ip)	The upper triangular sum of the detour Δ matrix	$Ip=\sum\Delta ij$ where the element Δ*ij* at the i,j-th position denotes the longest path linking vertex i with vertex j in the underlying graph (i, j = 1, 2, ... N) with N representing the total count of vertices
Electropy (Ie)	The summation of squared atomic nuclear charges divided by the square of one less than the total atom count in the molecule	$\varepsilon=1(\frac{p_a}{p_i})$ *pa* and *pi* signify the probabilities associated with the occurrence of an a priori event and an a posteriori event, respectively. A greater Ie index magnitude reflects a more electropositive character of the molecule.

The application of the topological (W) index enabled a direct comparison of the dimensions and morphology of graph-based carbon skeletons corresponding to saturated hydrocarbon segments within the Lvf structures under examination [22]. The (J) index, applied to a connected graph G, was used to derive distance matrices for molecular entities that incorporate multiple chemical bonds [23]. The greatest atom-to-atom separations within the molecular graph were accounted for via the traversal matrix Ip. In contrast, the matrix Ie captured contributions arising from spatial arrangements and electronic influences [24].

PASS

PASS (Prediction of Activity Spectra for Substances) Online (http://www.way2drug.com/passonline/ accessed on 21 June 2022) constitutes a computational platform designed to forecast the biological activity spectrum of submitted PMS and RMS structures by applying Pa (probability of being active) and Pi (probability of being inactive) metrics [25]. The ceiling activity value corresponds to the quotient Pa/Pi = 1, whilst a quantitative property estimate approaching zero (Pa/Pi → 0) was classified as "inactive". Functionally, PASS rests upon the dissection of molecular structure profiles using MNA descriptors (Multilevel neighborhoods of atoms) coupled with a Bayesian probabilistic framework for projecting the biological activity of molecular ligands [26]:

$$P(A_k|C) = P(C|A_k)\cdot P(A_k)/P(C), \quad (1)$$

In this expression, P(Ak|C) signifies the likelihood of encountering structure C under the condition that the compound exhibits activity Ak, P(Ak) designates the prior probability of activity Ak, and P(C) indicates the prior probability of structure C.

Within the PASS framework, the notion of equivalence is particularly significant: two structures are considered equivalent if they are represented by identical collections of MNA descriptors [27, 28].

Molecular docking software

The actual molecular configurations of the lead scaffold—levofloxacin—alongside computationally forecasted structural arrangements incorporating diverse bioisosteric substitutions and decomposition products, were assembled within the Avogadro 1.2.0 molecular builder (https://avogadro.cc/releases/avogadro_120/, accessed on 15 June 2016) [29]. Drawing on this refined editing platform, which rests on quantum-mechanical structural computations, subsequent geometric minimization of the small-molecule ligands was performed.

Contacts established between the low-molecular-weight ligands and the topoisomerase IIA fold were rendered using the PyMol 2.5 visualization package (https://pymol.org/2/, accessed on 1 October 2022) [30, 31].

The experimentally resolved coordinates of the topoisomerase IIA-DNA-6-FQ ternary assembly, originating from a bacterial source (Streptococcus pneumoniae topo IV-DNA-levofloxacin, PDB accession code: 3k9F), were adopted in line with the standardized validation documentation provided by the wwPDB X-ray Structure Validation Summary Report (https://pdbj.org/emnavi/disp.php?a=arch.valrep_pdb_sum.3k9f, accessed on 15 October 2009).

Preparatory handling of the macromolecular model entailed removal of the surrounding solvent environment and insertion of polar hydrogen atoms, operations conducted within the AutoDockTools 1.5.7 suite [32, 33]. Appending hydrogen atoms to the protein coordinate set sourced from the PDB and subsequently refining their spatial placement was the single most critical procedural undertaking [34].

The Achilles Blind Docking Server (https://bio-hpc.ucam.edu/achilles/, accessed on 25 January 2023), whose computational engine is driven by AutoDock Vina, pinpointed the binding disposition of the crystallographically characterized topoisomerase IIA with Lvf structural-derivative ligands while simultaneously computing the associated binding free energies [35, 36].

Autodock Vina achieves a performance leap of roughly two orders of magnitude over prior docking programs, while concurrently delivering a notable gain in the reliability of binding pose estimation. Supplementary acceleration is achieved through parallel execution, harnessing multithreading across multi-core processor architectures. Grid map computation and result clustering proceed entirely under automated control, without requiring user intervention [37, 38].

Apparatus for tribochemical treatment

A genuine (6-decarboxylated) chemical derivative of Lvf was generated via a tribochemical protocol that relied on forceful impact and shear loading applied to the solid phase [39]. For this undertaking, a Stegler LM-250 milling mechanoactivator equipped with a brush-type motor (Shenzhen Bestman Instrument CO., Ltd., Shenzhen, China), spinning at 28,000 rpm and delivering 13 kW of power, was used. The procedure for tribochemical processing of the levofloxacin powder involved filling the grinding receptacle with the substance suspension to roughly one-half of its total volume, then collecting the treated specimen following 21 minutes of sustained mechanical perturbation.

Fourier transform infrared spectroscopy

Collection of vibrational spectroscopic signatures for the levofloxacin RMS was performed using a Fourier transform infrared (FTIR) instrument (Agilent Cary 630, Santa Clara, CA, USA) equipped with a transmission sampling module, scanning the spectral region from 4000 to 400 cm^{-1}.

Optical microscopy (OM)

Particle morphology was assessed under an optical microscope equipped with a dedicated binocular observation head (Altami BIO 2, Saint Petersburg, Russia) at a total magnification of 10× (corresponding to a linear field width of 20 mm).

Statistical treatment of data

Statistical evaluation of all datasets employed Student's t-test alongside one-way analysis of variance (ANOVA) executed within the Origin Pro 2021 analytical package (https://www.originlab.com/2021, accessed on 15 January 2021). Differences were regarded as statistically meaningful at $P < 0.05$.

Results and Discussion

Probing the structure-activity relationship

To anticipate the biological activity spectrum of levofloxacin-related structures, a dual-pronged strategy was pursued: computational in silico manipulation to yield predicted Lvf structural variants, and tribological treatment of the bulk pharmaceutical powder to obtain a panel of authentic Lvf derivatives.

Computational experimentation (chemicpen, PASS online, chemdescript)

A «structure-activity» profiling exercise was carried out on a collection of uniformly predicted Lvf variants, ordered from the most to the least structurally elaborate among the FlrQ-3G series under study, as summarized in **Table 3**. The methodological approach adopted involved stepwise stripping of the most pharmacophorically significant functional appendages from the core scaffold to map the antimicrobial activity landscape.

Table 3. In silico prediction of the biological activity spectrum of levofloxacin derivatives.

№	Lvf structure derivatives	Prediction spectra of biological activity (Pa)						
		Ing TopII [1]*	Ing DNAS [2]*	SDAc [3]*	QnAnMc [4]*	AntBc [5]*	AntTt [6]*	Ing CYP1 A2 [7]*
1	basic 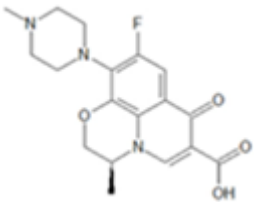	0.851	0.818	0.797	0.653	0.636	0.559	0
2	6-decarboxylated 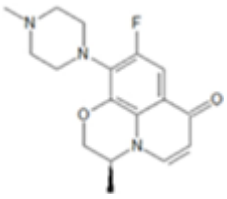	0.699	0.620	0.811	0.351	0.818	0.589	0.716
3	9-defluorinated 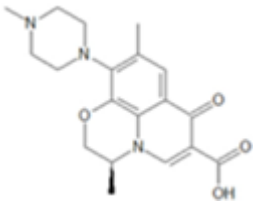	0.699	0.620	0.811	0.351	0.818	0.589	0.716
4	10-depyperazine 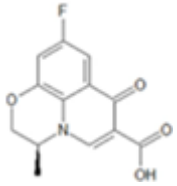	0.756	0.634	0.753	0.495	0.575	0.347	0.467
5	4-benzoxazine-BCS 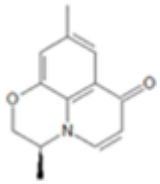	0.472	0.487	0.699	0.095	0.426	0.455	0.518
6	5-dehydro-4-benzoxazine-BCS 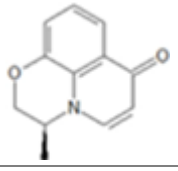	0.302	0.405	0.638	0.035	0.271	0.453	0.424

1—Type II DNA topoisomerase inhibitor that prevents ATP-dependent cleavage of both DNA chains of microbial cells. 2—inhibitor of the reparative and replicative DNA synthesis of microbial cells. 3—smart drug activities (Nootropics). 4—quinolone antimicrobial agent. 5—antibacterial agent. 6—antitumor activity. 7—cytochrome P-450 CYP1A2 isoform inhibitor.

A review of the tabulated figures indicates that, exceeding a probability cutoff of Pa > 0.8, the unmodified parent framework 1 shows—as anticipated—quinolone-type antimicrobial behavior, underpinned by type IIA

topoisomerase blockade and interference with bacterial DNA biosynthetic pathways. Consistent with the interpretation offered in [40], this indicates an 80% chance of a false rejection if one were to dismiss the premise that the Lvf molecule under examination indeed possesses this particular mode of action.

The projections of biological activity profiles obtained for congeners 2–4, all of which are devoid of the carboxyl at C6, the covalently linked fluorine substituent at C9, and the methylpiperazine ring at C10, prove to be especially revealing. A robust and sustained likelihood (Pa ≥ 0.7) of antibacterial effects driven by Ing TopII and Ing DNA synthesis functionalities remains intact. In tandem, the PASS software forecast hints at the emergence of smart-drug (nootropic) characteristics and cytochrome P-450 CYP1A2 inhibitory capacity—features not traditionally ascribed to FlrQ agents—falling within a Pa bracket of 0.5–0.8. Beyond this, the predicted activity patterns for quinolone variants 2 and 3 maintain unwavering quantitative confidence across all categories detailed in **Table 3**. This pattern may suggest an equal contribution of the structural descriptors embodied by the -COOH and -F substituents toward the «structure-activity» interplay characteristic of fluoroquinolones, a viewpoint echoed in the published record via the example of [41], in addition to their MNA equivalence.

When Lvf is subjected to yet more drastic structural truncation (variants 5 and 6), with only the rudimentary 4-benzoxazine-BCS nucleus preserved, the outcome is a near-certain obliteration of quinolone antimicrobial character (Pa < 0.1) and the vanishing of essentially all tabulated activity types, the sole exception being the smart drug property (Pa ~ 0.7). The nootropic activity signal returned by PASS for the fundamental oxa-azatricycloquinolone skeleton could conceivably serve as a springboard for the development of novel pharmaceutical agents capable of upregulating metabolic activity within central nervous system neuronal populations [42].

In an effort to tease out the dependency between the forecast biological activity spectrum and the molecular architecture of the cognate Lvf-predicted compounds, both integral and differential topological indices—well recognized for their exceptional discriminatory capability—were evaluated.

Two-dimensional (2D) graphical representations that capture the orderly trends in property shifts when contrasting distinct molecular graphs are supplied in **Figure 4**.

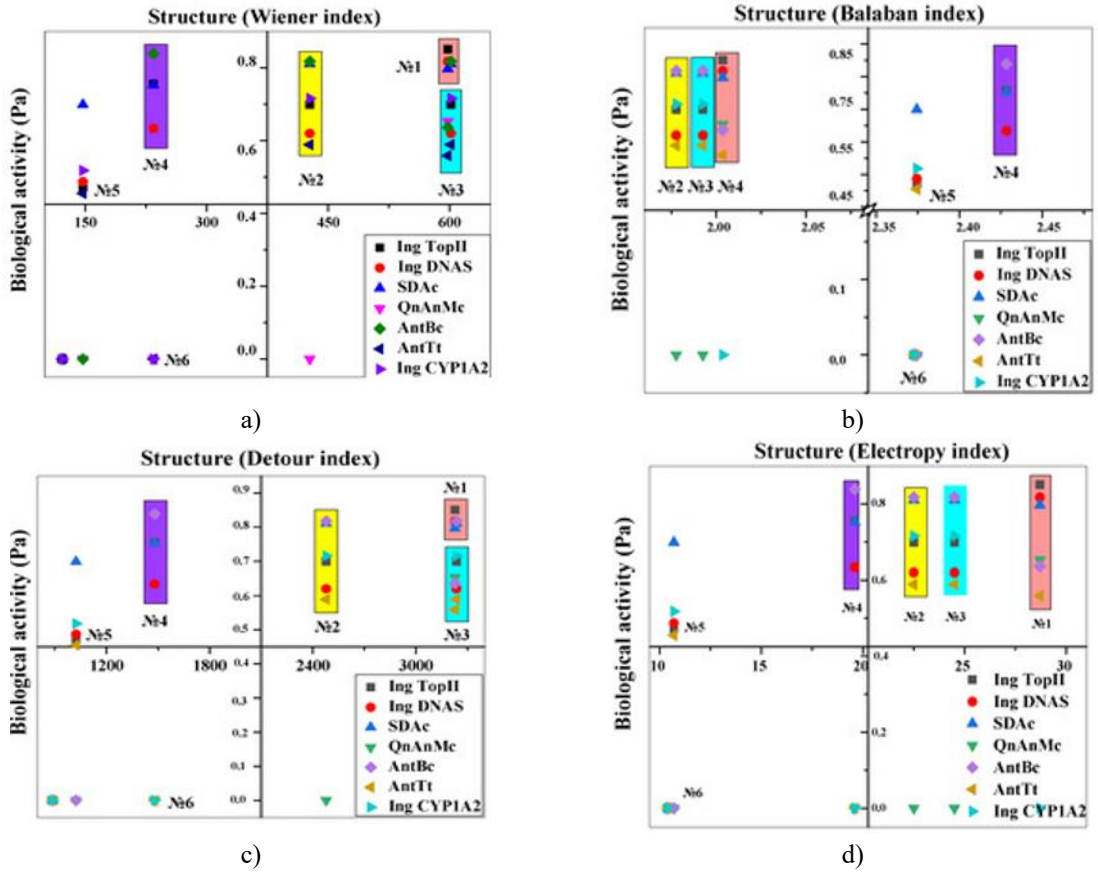

Figure 4. 2D diagrams of «structure-biological activity» relationship for the considered levofloxacin's predicted (№ 2–№6) derivatives relative to the real (№1) Lvf structure: (a) Wiener index; (b) Balaban index;

(c) Detour index; (d) Electropy index. The area structures: red—basic; blue—9-defluorinated; yellow—6-decarboxylated; violet—10-depyperazine. On the inserts—biological activity spectrum of predicted levofloxacin derivatives.

Inspection of the plots reveals that variants №1 (basic/real) and №3 (9-defluorinated) converge on a common point cluster associated with distinct biological activity modalities, with both lying within an overlapping span along the OX axis **(Figure 4a).** Given that the Wiener index (W) is derived from a distance matrix that captures graph bulk and topology, it stands to reason that, in terms of quantitative molecular characterization, no meaningful distinction separates structures №1 and №3. By contrast, variant №2, which corresponds to the 6-decarboxylated Lvf congener, populates a clearly demarcated zone, attesting to the uniqueness of its invariant molecular graph ensemble.

The progressive fragmentation of the fluoroquinolone molecular edifice (variants №4 and №5) yields firmly clustered points situated within an isolated sector that shows no overlap with the parent Lvf framework, once the nitrogen-containing base has been excised from the FlQns molecule. Variant №6, on the other hand, produces a haphazard dispersal of points across multiple territories, with no discernible preferential positioning. This phenomenon serves as a direct indicator of a collapsed «structure-activity» linkage. A matching picture across the entire panel of scrutinized structures was recorded upon calculation of the Detour (Ip) indices **(Figure 4c).** Turning to composite indices assembled by summing simpler component indices **(Table 2)** helps curb degeneracy and sharpen the resolving power for distinguishing chemical entities [43].

Deserving of closer examination is the 2D diagram that maps the dispersion of predicted biological activity magnitudes against the Balaban index. These computations lean upon the graph-theoretic notion of the graph center J(G) **(Figure 4b).** It becomes apparent that each forecast structure in the plot defines a unique coordinate within the diagram space. Concurrently, closely allied equivalent structures №1–№3 group together within a shared zone, whereas the 10-depyperazine variant (№4) stakes out an entirely separate territory. The Balaban index (J) exhibits a relatively restrained tendency toward degeneracy.

Topological indices correlate reasonably well with steric metrics (e.g., molecular volume, molecular surface extent) and with electronic attributes (e.g., ionization energies, electron affinities, polarizabilities, spin density distributions). By enlisting the aid of quantum chemical computations, supplementary details regarding the electron density arrangement within a molecule can be extracted through the Ie electropy index **(Figure 4d).**

Hence, the juxtaposition of topological indices in the dissection of related, chemically modified fluoroquinolone frameworks has brought to light not merely the reality of a «structure-activity» interdependence but also the reciprocal functional linkage amongst the topological indices (TIs) themselves. Among these, the Balaban and Electropy indices emerge as the most illuminating, low-degeneracy TIs suited for encoding the architectures and properties of Lvf derivatives.

Collectively, the set of 2D diagrams presented attests to the close structural and property-level kinship between the defluorinated analog and the parent scaffold. Both decarboxylation and defluorination of the Lvf blueprint slash the anticipated FlQns antimicrobial potency by roughly half. At the same time, these chemical alterations bring forth alternative “non-classical” biological signatures, most notably the suppression of the cytochrome P-450 CYP1A2 isoform. That being said, the decarboxylated derivative (dLvf) stands as the most discriminating model for reliably telling apart predicted equivalent levofloxacin structures when viewed through the lens of topological indices TI **(Figures 1 and 4).**

The authentic 6-decarboxylated Lvf architecture was generated using a tribochemical transformation-based technique.

Experimental work based on tribochemical activation

Localized thermal spikes generated at the interface of rubbing surfaces give rise to catalytically potent microenvironments that steer chemical transformation. In line with the catalytic scheme advanced in Kajdas [44], a sequence of low-energy electron expulsion, their interaction with molecular constituents populating the frictional boundary, and simultaneous thermionic release occurs in a stepwise fashion. Unsurprisingly, the unique convergence of physical events and chemical phenomena sets the stage for the initiation of a heterogeneous reaction pathway **(Figure 5)**.

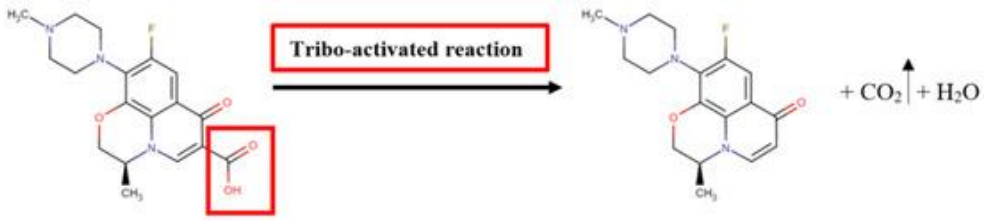

Figure 5. Tribochemical synthesis procedure of levofloxacine derivative. Conditions: 65 °C, 21 min, 13 kW of mechanical activator power.

Guided by the mechanistic regularities observed in non-thermal chemical conversions propelled by vigorous friction, shear deformation, and sustained static mechanical loading exerted upon solid matter, the resultant material—a decarboxylated congener of Lvf—underwent detailed examination via optical modalities of physicochemical assessment **(Figure 6)**.

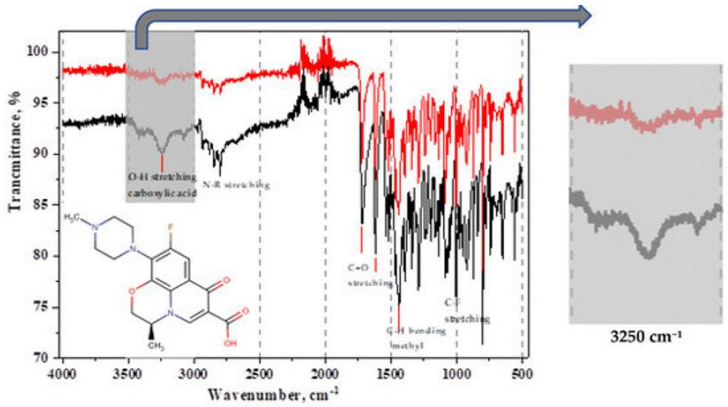

a)

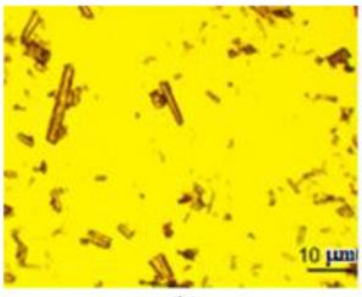

b)

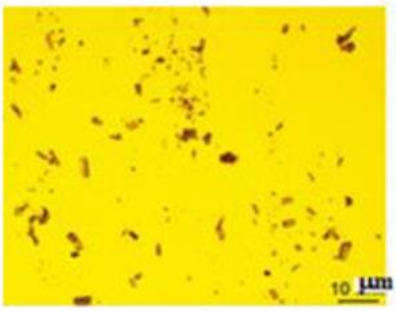

c)

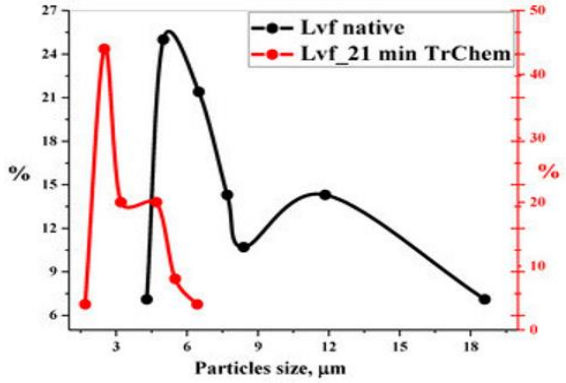

d)

Figure 6. A series of methods for qualitative, morphometric, and granulometry analysis of Lvf substance samples before and after tribochemical treatment. (a) FT−IR spectrometry, black—Lvf native, red—tribo-

activated Lvf (on a separate inset − region of O−H bond vibrations in the carboxyl group); (b,c) − optical microscopy (OM) of Lvf native and triboactivated substances, respectively; (d) OM granulometry for: black—Lvf native, red—triboactivated Lvf.

The experimental data reveal tangible shifts in the solid-state attributes induced by tribochemical exposure. Specifically, erosion of the characteristic needle-like crystalline morphology is evident, with the bulk of the particle population shifting to a size class centered at d = 5 μm. Those covalent bonds that have suffered distortion under the strain of high-energy tribochemical perturbation manifest a bathochromic displacement of their corresponding FT-IR absorption bands. The most conspicuous spectroscopic signature of bond degradation is the wholesale disappearance of the diagnostic high-frequency stretching mode belonging to the -OH hydroxyl proton of the carboxyl functionality, located in the vicinity of 3250 cm^{-1}.

Forecasting binding configurations and molecular modeling

Computational docking was used to predict how genuine and computationally predicted levofloxacin structural variants associate with discrete pockets on type IIA topoisomerase receptor proteins [45]. The small-molecule inhibitor was positioned within the quinolone resistance-determining region (QRDR) of the target genes, a stretch notorious for an elevated substitution rate in the QRDR segment of the GyrA subunit of DNA gyrase [46-48].

Graphical depiction of RMS, PMS compounds, and DNA Gyrase II docked poses

The sterically and energetically preferred binding postures, along with the corresponding conformations adopted by the low-molecular-weight ligands inside the receptor protein's catalytic cleft to yield tightly bound supramolecular assemblies, were mapped out. The locked three-dimensional (3D) spatial coordinates of the ligand-receptor couples belonging to structures №1–№4 **(Table 3)**—all of which registered a satisfactory QSAR trend during the preceding computational screening—are collected in **Figure 7**.

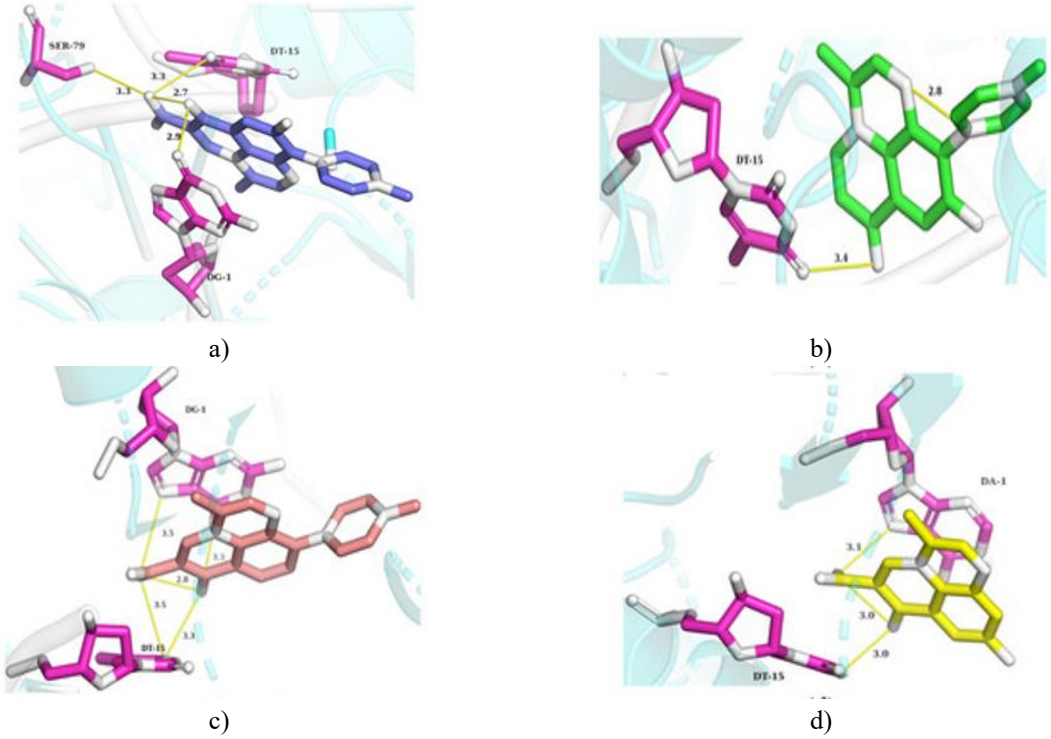

a) b) c) d)

Figure 7. Docking conformations obtained for different molecular structures of Lvf with specific regions of type IIA topoisomerase target proteins (with distances Å). H-bonds shown as yellow lines; non-polar hydrogen atoms have been removed for clarity [49]. (a)—basic Lvf; (b)—6-decarboxylated derivative; (c)—9-defluorinated derivative; (d)—10-depyperazine derivative.

Assessment of docking reliability was performed using the RMSD metric. For the 3K9F crystallographic entry, self-docking of the co-crystallized ligand proceeded without issue: the RMSD value separating the top-ranked

docked conformation from its experimentally frozen counterpart measures 0.986 Å. Such a modest discrepancy (comfortably beneath the conventionally accepted ceiling of 2 Å) between the predicted pose and the crystallographic reference underscores the capacity of the docking routine applied herein to faithfully recapitulate the spatial architecture of molecular recognition events.

As the structural snapshots indicate **(Figure 7),** the interfacial contact patches forged between the RMS and PMS low-molecular-weight ligands and the functionally essential amino acid residues adorning the protein-receptor binding site—identified as SER-79 (serine), DT-15 (deoxythymidine), DG-1 (deoxyguanosine), and DA-1 (deoxyadenosine)—are realized through both intra- and inter-molecular tethering points featuring the -OH and C=O groups of the carboxyl substituent at C6, the carbonyl oxygen C=O at C7, and the C-O-C ether linkage embedded within the 4-benzoxazine-BCS fragment, all operating via hydrogen-bond-mediated contacts.

Inspection of the illustrated 3D models reveals that the complex involving the native carboxyl-bearing ligand enjoys the richest network of binding interactions arrayed across the spatial landscape **(Figure 7a)**. Furthermore, several amino acid side-chain residues become engaged in the supramolecular assemblies formed between the target macromolecule—bacterial type IIA topoisomerases—and both the 9-defluorinated derivative and the 10-depyperazine Lvf analog **(Figures 7c and 7d)**. The additive effect of these contributions translates into a more robust tethering of the ligand inside the receptor protein's active site cavity [50].

Turning to the decarboxylated RMS binding orientation, the ligand's carbonyl oxygen, along with the deoxythymidine base (adopting its lactim tautomeric form), cooperates in establishing intermolecular contacts that cement the complex. Meanwhile, the oxygen atom -O- situated within the 4-benzoxazine-BCS scaffold engages in an intramolecular hydrogen-bonding interaction with the hydrogen atom appended to C2 of the 4-methylpiperazin-1-yl substituent.

To perform geometry-based scoring of ligand-receptor pairing, Autodock Vina draws upon an empirical energy function made up of a pair of Gaussian expressions supplemented by terms accounting for steric clash, hydrophobic desolvation effects, and hydrogen bond formation [51, 52]. **Table 4** lists the empirical scoring function components used to obtain a semi-quantitative estimate of the binding affinity of a ligand-receptor complex after docking. The average fractional contribution of each interaction class to the overall predicted binding energy (affinity, reported in kcal/mol) is shown as a percentage.

Table 4. Empirical scoring function weights and terms.

Ligand	Steric interaction (Gauss 1)	Steric interaction (Gauss 2)	Non-steric interaction (Repulsion)	Non-steric interaction (Hydrophobic attraction)	Non-steric interaction (Non-directional hydrogen bond)	Affinity values, kcal/mol
basic Lvf	7.50	91.97	0.16	0.29	0.08	−9.7
9-defluorinated	7.67	91.74	0.17	0.31	0.11	−9.4
6-decarboxylated	7.35	92.17	0.12	0.33	0.03	−8.9
10-depyperazine	8.66	90.84	0.19	0.19	0.12	−8.6

The scoring function is a weighted sum in which steric interaction contributions occupy the first three slots in **Table 4**, while the term describing hydrophobic contacts between non-polar atoms and the hydrogen bonding expression fill the final two positions in **Table 4**.

Estimation of the protein-ligand system's binding constant is carried out via the AutoDock Vina platform (autodock.scripps.edu. Date of access: 15 May 2016), which transforms affinity energy quantities (expressed in kcal/mol) into Kb following the relationship detailed hereafter:

$$\Delta G^{0}_{bind} = -RTlnK_b \quad (2)$$

$$K_b = \exp exp\left(\frac{-\Delta G_{bind}}{RT}\right) \quad (3)$$

$$K_b = K_d^{-1} \quad (4)$$

In this expression, $\Delta G^{0}_{\text{bind}}$ corresponds to the standard free energy liberated upon "protein-ligand" association (kcal/mol), R is the universal gas constant (8.314×10^{-3} kJ/K·mol), T is held at 298 K (25 °C), Kb designates the binding constant (M^{-1}), and Kd refers to the dissociation constant (M).

For each converged docking solution, clustering output becomes accessible in the form of ligand coordinate sets positioned within the target protein's active pocket, plotted relative to the global energetic trough of the assembled complex. Those binding orientations with the most favorable docking scores were singled out to identify the top-populated clusters retrospectively after docking, using the AutoDockTools 1.5.7 suite (see Section 2.4). The ensuing datasets afford predictive insight into the operative binding mechanism **(Figure 8; Table 5).**

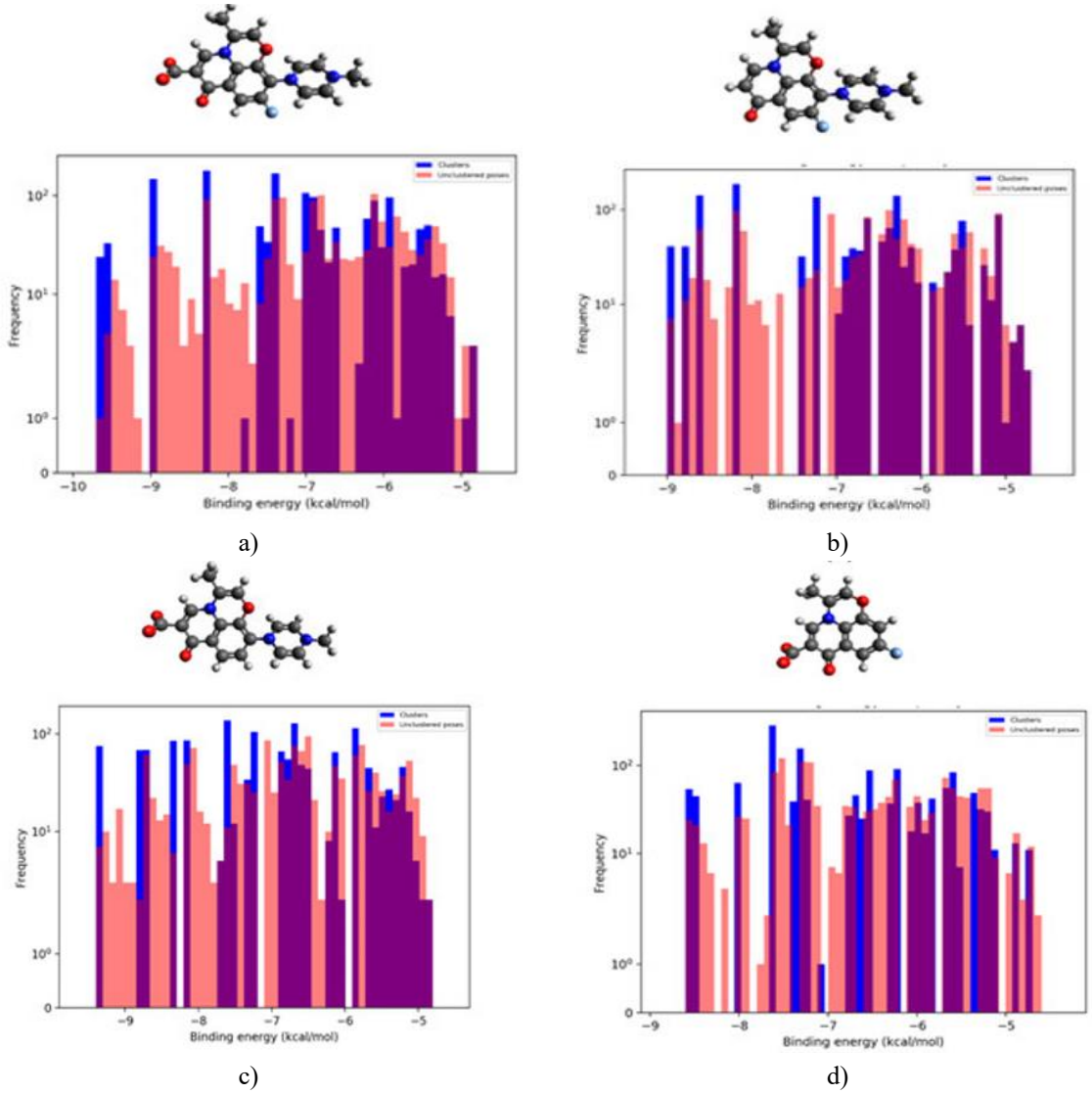

Figure 8. Clustering diagrams: (a) basic levofloxacin; (b) 6−decarboxylated derivative; (c) 9−defluorinated derivative; (d) 10−depyperazine derivative (the purple areas of the diagrams show the number of low population clusters). On the upper insets—the ligand images after processing the molecular editor Avogadro 1.2.0; atoms of elements are highlighted by color: dark gray—C, light gray—H, blue—N, red—O.

Table 5. Clustering data.

Ligand	Poses in cluster	Best pose	Binding site coordinates	$K_b \cdot 10^5$, M^{-1}
basic levofloxacin	24	592	(−22.18, 50.92, −37.92)	1.31
	33	1201	(−39.00, 54.45, −38.88)	
	69	232	(−18.02, 26.50, −36.81)	
9-defluorinated	36	982	(−22.25, 51.62, −38.84)	1.30
	39	591	(−39.10, 54.89, −38.22)	
	68	173	(−18.43, 27.23, −36.66)	
6-decarboxylated	41	1228	(−39.16, 54.97, −38.91)	1.29
	41	1001	(−22.00, 51.04, −38.77)	
	66	258	(−17.54, 26.57, −36.31)	

10-depyperazine	54	1223	(−38.84, 54.74, −37.11)	1.28
	45	592	(−22.03, 51.80, −37.31)	
	37	985	(−18.27, 55.28, −25.49)	

The cluster frequency histogram reports the number of binding conformations mapped at various binding energy strata. A set of clusters with elevated occupancy typically indicates that the docking protocol was executed in a well-converged and reliable manner [53, 54].

What the cluster analysis brings into sharp relief are pronounced disparities between the predicted molecular arrangement of the 10-depyperazine species and the native levofloxacin backbone, as well as the remainder of the PMS series. The maximal Gibbs free energy value, paired with a higher cluster count and a broader spread of low-molecular-weight ligand conformations populating the binding cavity, implies unsatisfactory performance in locating the complex's low-energy basin. The 9-defluorinated analog, on the other hand, mirrors the parent levofloxacin scaffold quite faithfully, both in terms of the low-energy minimum profile and the Kb magnitudes. A clear parallel with the QSAR trends emerging from the in silico experiment can be traced at this juncture **(Figure 4)**.

As one might reasonably expect, the 6-decarboxylated congener—obtained via the TrbCh methodology and forming the sparsest set of contacts, limited to a solitary amino acid side chain DT-15—shows a comparatively weaker docking fidelity **(Table 4)**. This finding reinforces the concept that fluoroquinolone behavior is intimately tied to the presence of a carboxyl-bearing architecture **(Figures 1 and 2).**

Conclusion

This investigation showcases the deployment of in silico methodologies to pinpoint quantitative structure-activity relationships, illustrated through the case of real (RMS) and predicted (PMS) levofloxacin forms. The biological activity landscape of levofloxacin congeners, ranked by decreasing structural complexity and compared with the parent levofloxacin, was charted using a Bayesian probabilistic model. It was revealed that excising the carboxyl functionality from the molecular blueprint halves the projected FlQns' antimicrobial efficacy. In parallel, these structural modifications call forth additional "non-classical" biological traits, above all the inhibition of the cytochrome P-450 isoform CYP1A2. The Balaban and Electropy descriptors emerge as the richest in information content and the least susceptible to degeneracy among the topological indices for depicting and segregating RMS and PMS Lvf variants. Based on the 2D graphical displays, the native and defluorinated Lvf structures are closest to one another. Harnessing the capabilities of modern-generation molecular docking packages (AutoDockTools 1.5.7 coupled with the next-generation engine Autodock Vina), the biologically promising levofloxacin candidates flagged by the QSAR screening were rendered as 3D models of the respective ligand-receptor adducts. Anchored in the empirical scoring function, the final predicted binding energy (affinity, kcal/mol), the binding constants Kb (M^{-1}), and the insights extracted from the cluster diagrams jointly attested to the near-identity of the 9-defluorinated Lvf species relative to the original levofloxacin. The knowledge generated has applied value in the development of pharmaceutical agents with intentionally tailored properties, starting from an established lead compound and a well-characterized active site of the target protein [55].

Acknowledgments: The authors would like to thank Vladimir B. Sulimov—the head of the Research Computing Center Laboratory at Lomonosov Moscow State University —for advice on molecular modeling.

Conflict of Interest: None

Financial Support: This research has been supported by the RUDN University Strategic Academic Leadership program grant number 033320-0-000.

Ethics Statement: None

References

1. Vidyavathi M, Srividya G. A review on ciprofloxacin: dosage form perspective. Int J Appl Pharm. 2018;10:6-10.

2. Center for Drug Evaluation and Research. FDA updates warnings for oral and injectable fluoroquinolone antibiotics [Internet]. Silver Spring (MD): U.S. Food and Drug Administration; 2018 [cited 2016 May 12]. Available from: https://www.fda.gov/drugs/drug-safety-and-availability/fda-updates-warnings-oral-and-injectable-fluoroquinolone-antibiotics
3. Dey BK, Myrsing E, Amin R, Alam F, Rahman M, Gogol P, et al. A ripple effect of COVID-19 pandemic on shortage of medicinal products and its impact on patient care. Int J Appl Pharm. 2021;13:364-70.
4. Rusu A, Munteanu AC, Arbănași EM, Uivarosi V. Overview of side-effects of antibacterial fluoroquinolones: new drugs versus old drugs, a step forward in the safety profile? Pharmaceutics. 2023;15:804.
5. Spencer AC, Panda SS. DNA gyrase as a target for quinolones. Biomedicines. 2023;11:371.
6. Millanao AR, Mora AY, Villagra NA, Bucarey SA, Hidalgo AA. Biological effects of quinolones: a family of broad-spectrum antimicrobial agents. Molecules. 2021;26:7153.
7. Ray GT, Baxter R, DeLorenze GN. Hospital-level rates of fluoroquinolone use and the risk of hospital-acquired infection with ciprofloxacin-nonsusceptible Pseudomonas aeruginosa. Clin Infect Dis. 2005;41:441-9.
8. Kishii R, Yamaguchi Y, Takei M. In vitro activities and spectrum of the novel fluoroquinolone lascufloxacin (KRP-AM1977). Antimicrob Agents Chemother. 2017;61:e00120-17.
9. Bhagwat SS, Nandanwar M, Kansagara A, Patel A, Takalkar S, Chavan R, et al. Levonadifloxacin, a novel broad-spectrum anti-MRSA benzoquinolizine quinolone agent: review of current status. Drug Des Devel Ther. 2019;13:4351-65.
10. Bridle MJ, Janesko BG. Computational study of fluoroquinolone binding to $Mg(H_2O)n^{2+}$ and its applicability to future drug design. Int J Quantum Chem. 2017;117:e25428.
11. Bush NG, Diez-Santos I, Abbott LR, Maxwell A. Quinolones: mechanism, lethality and their contributions to antibiotic resistance. Molecules. 2020;25:5662.
12. Rusu A, Lungu IA, Moldovan OL, Tanase C, Hancu G. Structural characterization of the millennial antibacterial (fluoro)quinolones—shaping the fifth generation. Pharmaceutics. 2021;13:1289.
13. National Center for Biotechnology Information. PubChem compound summary for lascufloxacin [Internet]. Bethesda (MD): National Library of Medicine; [cited 2023 Jun 23]. Available from: https://pubchem.ncbi.nlm.nih.gov/compound/Lascufloxacin
14. Dayam R, Al-Mawsawi LQ, Zawahir Z, Witvrouw M, Debyser Z, Neamati N. Quinolone 3-carboxylic acid pharmacophore: design of second generation HIV-1 integrase inhibitors. J Med Chem. 2008;51:1136-44.
15. Stern E, Muccioli GG, Millet R, Goossens JF, Farce A, Chavatte P, et al. Novel 4-oxo-1,4-dihydroquinoline-3-carboxamide derivatives as new CB2 cannabinoid receptor agonists: synthesis, pharmacological properties and molecular modeling. J Med Chem. 2006;49:70-9.
16. Manera C, Benetti V, Castelli MP, Cavallini T, Lazzarotti S, Pibiri F, et al. Design, synthesis, and biological evaluation of new 1,8-naphthyridin-4(1H)-on-3-carboxamide and quinolin-4(1H)-on-3-carboxamide derivatives as CB2 selective agonists. J Med Chem. 2006;49:5947-57.
17. Zhu L, Zhang Y, Yang J, Wang Y, Zhang J, Zhao Y, et al. Prediction of the pharmacokinetics and tissue distribution of levofloxacin in humans based on an extrapolated PBPK model. Eur J Drug Metab Pharmacokinet. 2016;41:395-402.
18. Krishnan SR, Bung N, Vangala SR, Srinivasan R, Bulusu G, Roy A. De novo structure-based drug design using deep learning. J Chem Inf Model. 2022;62:5100-9.
19. National Center for Biotechnology Information. PubChem compound summary for levofloxacin [Internet]. Bethesda (MD): National Library of Medicine; [cited 2023 Jun 23]. Available from: https://pubchem.ncbi.nlm.nih.gov/compound/Levofloxacin
20. Informer Technologies Inc. ChemicPen [Internet]. [cited 2022 Oct 21]. Available from: https://chemicpen.software.informer.com
21. Randić M, Sabljić A, Nikolić S, Trinajstić N. A rational selection of graph-theoretical indices in the QSAR. Int J Quantum Chem. 1988;34:267-85.
22. Balaban AT. Topological indices and their uses: a new approach for the coding of alkanes. J Mol Struct THEOCHEM. 1988;165:243-53.
23. Gopika S, Lakshmi A, Aiswarya PD, Rajendran S. On the detour based indices. Math Stat Eng Appl. 2022;71:951-66.

24. Fang W, Liu WH, Liu JB, Chen FY, Hong ZM, Xia ZJ. Maximum detour-Harary index for some graph classes. Symmetry. 2018;10:608.
25. Filimonov DA, Lagunin AA, Gloriozova TA. Prediction of the biological activity spectra of organic compounds using the PASS online web resource. Chem Heterocycl Compd. 2014;50:444-57.
26. Fomenko AE, Sobolev BN, Filimonov DA, Poroikov VV. Use of structural MNA descriptors for designing profiles of protein families. Biophysics. 2003;48:595-605.
27. Dmitriev AV, Rudik AV, Karasev DA, Pogodin PV, Lagunin AA, Filimonov DA, et al. In silico prediction of drug-drug interactions mediated by cytochrome P450 isoforms. Pharmaceutics. 2021;13:538.
28. Filimonov DA, Druzhilovskiy DS, Lagunin AA, Gloriozova TA, Rudik AV, Dmitriev AV, et al. Computer-aided prediction of biological activity spectra for chemical compounds: opportunities and limitations. Biomed Chem Res Methods. 2018;1:e00004.
29. Hanwell MD, Curtis DE, Lonie DC, Vandermeersch T, Zurek E, Hutchison GR. Avogadro: an advanced semantic chemical editor, visualization, and analysis platform. J Cheminform. 2012;4:17.
30. Maschietto F, Allen B, Kyro GW, Batista VS. MDiGest: a Python package for describing allostery from molecular dynamics simulations. J Chem Phys. 2023;158:215103.
31. Rosignoli S, Di Paola L, Paiardini A. PyPCN: protein contact networks in PyMOL. Bioinformatics. 2023;39:btad675.
32. Morris GM, Huey R, Lindstrom W, Sanner MF, Belew RK, Goodsell DS, et al. AutoDock4 and AutoDockTools: automated docking with selective receptor flexibility. J Comput Chem. 2009;30:2785-91.
33. Eberhardt J, Santos-Martins D, Tillack AF, Forli S. AutoDock Vina 1.2.0: new docking methods, expanded force field, and Python bindings. J Chem Inf Model. 2021;61:3891-8.
34. Sulimov VB, Kutov DC, Taschilova AS, Ilin IS, Tyrtyshnikov EE, Sulimov AV. Docking paradigm in drug design. Curr Top Med Chem. 2021;21:507-46.
35. Vieira TF, Sousa SF. Comparing AutoDock and Vina in ligand/decoy discrimination for virtual screening. Appl Sci. 2019;9:4538.
36. Zhou X, Ling M, Lin Q, Tang S, Wu J, Hu H. Effectiveness analysis of multiple initial states simulated annealing algorithm: a case study on the molecular docking tool AutoDock Vina. IEEE ACM Trans Comput Biol Bioinform. 2023;20:1-12. doi:10.2139/ssrn.4120348
37. Trott O, Olson AJ. AutoDock Vina: improving the speed and accuracy of docking with a new scoring function, efficient optimization, and multithreading. J Comput Chem. 2010;31:455-61.
38. Agarwal R, Smith JC. Speed vs accuracy: effect on ligand pose accuracy of varying box size and exhaustiveness in AutoDock Vina. Mol Inform. 2023;42:e2200188.
39. Uspenskaya E, Simutina A, Kuzmina E, Sukhanova V, Garaev T, Pleteneva T, et al. Exploring the effects of cramped-impact-type mechanical action on active pharmaceutical ingredient (levofloxacin): prospects for pharmaceutical applications. Powders. 2023;2:464-83.
40. Lagunin A, Stepanchikova A, Filimonov D, Poroikov V. PASS: prediction of activity spectra for biologically active substances. Bioinformatics. 2000;16:747-8.
41. He QQ, Zhang X, Yang LM, Zheng YT, Chen F. Synthesis and biological evaluation of 5-fluoroquinolone-3-carboxylic acids as potential HIV-1 integrase inhibitors. J Enzyme Inhib Med Chem. 2012;28:671-6.
42. Malík M, Tlustoš P. Nootropics as cognitive enhancers: types, dosage and side effects of smart drugs. Nutrients. 2022;14:3367.
43. Stankevich MI, Stankevich IV, Zefirov NS. Topological indices in organic chemistry. Russ Chem Rev. 1998;57:191-208.
44. Kajdas C. General approach to mechanochemistry and its relation to tribochemistry. Tribol Eng. 2013;11:209-30.
45. Maeda Y, Kiba A, Ohnishi K, Hikichi Y. Implications of amino acid substitutions in GyrA at position 83 in terms of oxolinic acid resistance in field isolates of Burkholderia glumae, a causal agent of bacterial seedling rot and grain rot of rice. Appl Environ Microbiol. 2004;70:5613-20.
46. Tang K, Zhao H. Quinolone antibiotics: resistance and therapy. Infect Drug Resist. 2023;16:811-20.
47. Shaheen A, Tariq A, Iqbal M, Mirza O, Haque A, Walz T, et al. Mutational diversity in the quinolone resistance-determining regions of type-II topoisomerases of Salmonella serovars. Antibiotics (Basel). 2021;10:1455.

48. Mehla K, Ramana J. Structural signature of Ser83Leu and Asp87Asn mutations in DNA gyrase from enterotoxigenic Escherichia coli and impact on quinolone resistance. Gene. 2016;576:28-35.
49. Liu J, Zhang H, Xiao Z, Wang F, Wang X, Wang Y. Combined 3D-QSAR, molecular docking and molecular dynamics study on derivatives of peptide epoxyketone and tyropeptin-boronic acid as inhibitors against the β5 subunit of human 20S proteasome. Int J Mol Sci. 2011;12:1807-35.
50. Li L, Ji J, Song F, Hu J. Intercellular receptor-ligand binding: effect of protein-membrane interaction. J Mol Biol. 2023;435:167787.
51. Min X, Cheng S, Yang J, Qing W, Niu H. Systematic investigation of docking failures in large-scale structure-based virtual screening. ACS Omega. 2022;7:39417-28.
52. Quiroga R, Villarreal M. Vinardo: a scoring function based on AutoDock Vina improves scoring, docking, and virtual screening. PLoS One. 2016;11:e0155183.
53. Sulimov VB, Sulimov AV. Docking: Molecular Modeling for Drug Discovery. Moscow: AINTELL; 2017.
54. Suvannang N, Nantasenamat C, Isarankura-Na-Ayudhya C, Prachayasittikul V. Molecular docking of aromatase inhibitors. Molecules. 2011;16:3597-617.
55. Novichikhina NP, Shestakov AS, Medvedeva SM, Lagutina AM, Krysin MY, Podoplelova NA, et al. New hybrid tetrahydropyrrolo[3,2,1-ij]quinolin-1-ylidene-2-thioxothiazolidin-4-ones as new inhibitors of factor Xa and factor XIa: design, synthesis, and in silico and experimental evaluation. Molecules. 2023;28:3851.